
Article:
Ben, L., Li, L., Harding, J.H. orcid.org/0000-0001-8429-3151 et al. (2 more authors) (2022) Tuning the electrical conductivity of Rare Earth-doped BaTiO3 using Gd2O3 as an exemplar. Open Ceramics, 9. 100250.

https://doi.org/10.1016/j.oceram.2022.100250

Open Ceramics 9 (2022) 100250

Contents lists available at ScienceDirect

Open Ceramics

journal homepage: www.sciencedirect.com/journal/open-ceramics

Tuning the electrical conductivity of Rare Earth-doped $BaTiO_3$ using Gd_2O_3 as an exemplar

Liubin Ben [a,b], Linhao Li [a], John H. Harding [a], Colin L. Freeman [a], Derek C. Sinclair [a,*]

[a] Department of Materials Science and Engineering, Sir Robert Hadfield Building, University of Sheffield, Mappin Street, Sheffield, S1 3JD, United Kingdom
[b] Beijing National Laboratory for Condensed Matter Physics, Institute of Physics, Chinese Academy of Sciences, Beijing, 100190, China

ARTICLE INFO

Keywords:
Barium titanate
Rare earth doping
Defect chemistry
Impedance spectroscopy

ABSTRACT

The electrical properties of Gd-doped $BaTiO_3$ ceramics prepared by various doping mechanisms have been investigated using Impedance Spectroscopy and correlated with the proposed doping mechanisms observed from phase diagram studies and with solution energies obtained from atomistic simulations. Undoped $BaTiO_3$, $BaTi_{1-x}Gd_xO_{3-x/2}$, $Ba_{1-y/2}Ti_{1-y/2}Gd_yO_3$ and $Ba_{1-z}Gd_zTi_{1-z/4}O_3$ were prepared. The first two series and $y < 0.10$ samples possess extrinsic p-type conduction due to oxygen gain (oxidation) associated with the presence of oxygen vacancies. A core-shell microstructure causes electrical heterogeneity where $y < 0.10$. For $y \geq 0.10$, oxygen vacancies are eliminated by substitution of a small excess of Gd^{3+} at the Ba-site leading to intrinsic (band-type) conduction. All $Ba_{1-z}Gd_zTi_{1-z/4}O_3$ ceramics processed in air exhibit n-type semiconductivity that is attributed to a small amount of oxygen loss (reduction) during sintering. The oxygen loss can be prevented by processing ceramics in a flowing O_2 atmosphere.

1. Introduction

The influence of impurities, dopants and materials processing on the defect chemistry and how they control the electrical properties of functional oxides is an important and challenging topic. It generally requires a multi-technique approach based on a combination of experimental and modelling methods that can collectively elucidate structure-composition-property relationships. A useful example is the ferroelectric perovskite (ABO_3) barium titanate which (in various doped forms) finds numerous commercial applications as an electroceramic. These include as a high permittivity dielectric material in Multi-Layer Ceramic Capacitors (MLCCs) [1–3] and as a positive temperature coefficient of resistance (ptcr) device [4] in current-limiting and temperature-sensing applications. The former relies on both the grain and grain boundary regions being electrically insulating whereas the latter relies on the development of Schottky-type barriers between semiconducting (n-type) grains and insulating grain boundaries [5,6].

It is instructive to consider first the electrical properties of the undoped parent compound and how they are influenced by low levels of impurities in the starting reagents and/or via ceramic processing conditions. For example, changing the purity of Fe_2O_3 (99.8 vs 99.99%) used in the mixed oxide preparation of $LaFeO_3$ (LF) induces a switch from n-to p-type behaviour. The higher levels of impurities associated with the 99.8% Fe_2O_3 'mask' the intrinsic defect chemistry (in air) of LF [7,8]. High energy milling in the form of attrition milling can induce impurity contamination that can be avoided if lower energy milling processes are employed, e.g. hand grinding using an agate mortar and pestle, or if the time employed for high energy milling is restricted. Studies have shown that attrition milling of undoped $BaTiO_3$ powders from 0.5 to 3 h in Y-doped ZrO_2-based milling media can result in partial replacement of Ba with Y on the A-sites and Ti with Zr on the B-sites [9]. This causes a reduction in the ferroelectric Curie temperature and a decrease in the electrical conductivity. Long milling periods (e.g. 3 hrs) can stabilise the rhombohedral polymorph of BT at room temperature (RT), as opposed to the expected tetragonal polymorph.

'Ideal' or impurity/defect free '$BaTiO_3$' would contain Ba and Ti in their fully oxidised states (i.e. Ba^{2+}, $6s^0$ and Ti^{4+}, $3d^0$) and O in its fully reduced state (i.e. O^{2-}, $2s^22p^6$) and be electrically insulating at room temperature with resistivity ~10 GΩ cm. The intrinsic bulk (grain) conduction mechanism at elevated temperatures (e.g. ~ 300 °C) will arise from promotion of electrons from the valence band to the conduction band,

$$nil \rightarrow e' + h^{\bullet} \quad (1)$$

* Corresponding author.
E-mail address: d.c.sinclair@sheffield.ac.uk (D.C. Sinclair).

https://doi.org/10.1016/j.oceram.2022.100250
Received 15 December 2021; Received in revised form 25 February 2022; Accepted 16 March 2022
Available online 23 March 2022

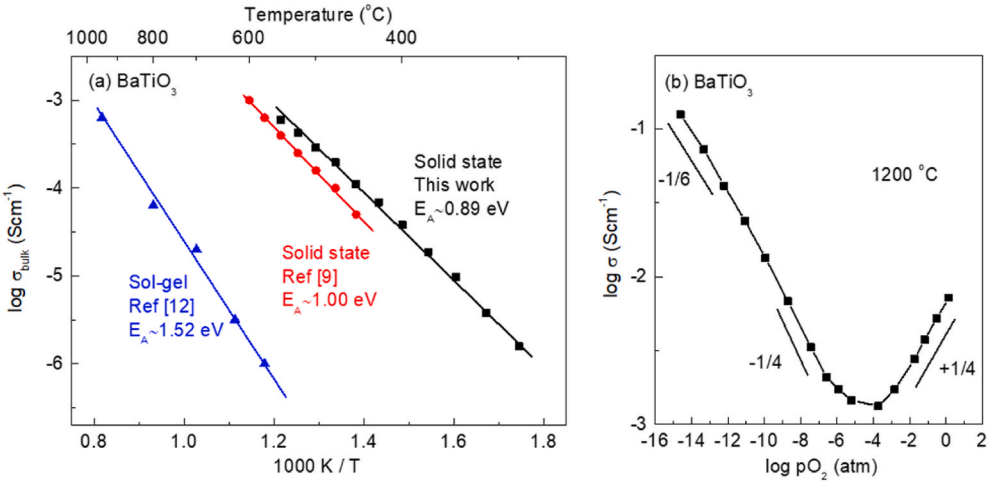

Fig. 1. (a) Arrhenius plots of bulk conductivity, σ_b, obtained from $BaTiO_3$ ceramics prepared by different routes: ball milling (black squares, this work); attrition milling (red circles, ref [9]); sol-gel (blue triangles, ref [12]. (b) Schematic of log σ_b versus log oxygen partial pressure, Po_2 for undoped $BaTiO_3$ at 1200 °C. (For interpretation of the references to colour in this figure legend, the reader is referred to the Web version of this article.)

with a typical activation energy, E_A of 1.50 eV, which is approximately half the optical band gap, E_g, of 3.2 eV [10]. This E_A has been reported for the bulk conductivity, σ_b, of $BaTiO_3$ prepared by methods that involve very low levels of impurities e.g. a sol-gel process and processing by hand grinding (to avoid contamination from milling media) using a mortar and pestle [11,12]. However, $BaTiO_3$ ceramics are more commonly prepared by a solid state (mixed oxide) route using ball milling [9,13] and, although they remain electrically insulating at RT, σ_b at elevated temperatures is several orders of magnitude higher with a lower E_A of 0.6–1.0 eV compared to sol-gel derived samples, Fig. 1 (a). This lower E_A and extrinsic p-type conduction has been explained on the basis of the following oxidation reaction

$$V_O^{\bullet\bullet} + 1/2O_2 \rightarrow O_O^{\times} + 2h^{\bullet} \quad (2)$$

where the oxygen vacancies, $Vo^{\bullet\bullet}$, being filled originate from incorporation of accidental impurities, such as Fe and Al (typically in the range of ~100 s ppm) in starting compositions because of their natural abundance in reagent grade TiO_2 [10,14]. In these, nominally undoped, '$BaTiO_3$' materials the impurities A^{3+} (where $A^{3+} = Fe^{3+}$, Al^{3+}) act as B-site acceptors and substitute at the Ti-site with charge compensation by oxygen vacancies based on the following equation

$$A_2O_3 + 2BaO \rightarrow 2Ba_{Ba}^{\times} + 2A_{Ti}^{'} + 5O_O^{\times} + V_O^{\bullet\bullet} \quad (3)$$

Only a low level of $Vo^{\bullet\bullet}$ is filled by mechanism (2) but this is sufficient to produce the p-type behaviour of 'undoped' $BaTiO_3$ ceramics. The mobility of $Vo^{\bullet\bullet}$ at RT and in low electric fields is low and therefore the contribution of oxide-ion conduction to σ_b near RT is very low. This acceptor-doped impurity model was developed by Smyth and co-workers and is reviewed in more rigorous detail in Refs. [14,15]. The interactions between $Vo^{\bullet\bullet}$ and larger electrical fields is an important topic in the pre- and high field-breakdown mechanisms that can occur in $BaTiO_3$-based materials. This is beyond the scope of this review but the interested reader is referred to Ref. [3] for more details.

The above describes the situation for p-type oxidised ceramics processed (sintered and cooled) in ambient air; however, when processing in lower oxygen partial pressures, Po_2, (e.g. 5% H_2 at 1300 °C) undoped $BaTiO_3$ can undergo the following reduction reaction

$$O_O^{\times} \rightarrow 1/2O_2 + V_O^{\bullet\bullet} + 2e^{'} \quad (4)$$

where $Vo^{\bullet\bullet}$ and conduction electrons are created due to the loss of lattice oxygen [8]. Cooling under this low Po_2 to prevent reoxidation produces blue-black ceramics (due to partial reduction of some Ti^{4+} (d^0) to Ti^{3+} (d^1) ions) that are now n-type semiconducting with RT resistivity ~ 10^1–10^4 Ωcm. The E_A associated with n-type σ_b is typically ~0.05–0.10 eV.

Table 1
Possible charge compensation routes for Gd-doped $BaTiO_3$.

Doping site	Compensation mechanism	Kröger-Vink equation & Chemical formula	
A-site	Ionic	$2Gd_2O_3 + 4Ba_{Ba}^{\times} + Ti_{Ti}^{\times} \rightarrow 4Gd_{Ba}^{\bullet} + V_{Ti}^{'''} + 4BaO + TiO_2$ $Ba_{1-z}Gd_zTi_{1-z/4}O_3$	i
	Ionic	$Gd_2O_3 + 3Ba_{Ba}^{\times} \rightarrow 2Gd_{Ba}^{\bullet} + V_{Ba}^{'} + 3BaO$ $Ba_{1-3a/2}Gd_aTiO_3$	ii
	electronic	$Gd_2O_3 + 2Ba_{Ba}^{\times} \rightarrow 2Gd_{Ba}^{\bullet} + 2e^{'} + 2BaO + 1/2O_2\uparrow$ $Ba_{1-b}Gd_bTiO_3$	iii
B-site	ionic	$Gd_2O_3 + 2Ti_{Ti}^{\times} + O_O^{\times} \rightarrow 2Gd_{Ti}^{'} + V_O^{\bullet\bullet} + 2TiO_2$ $BaTi_{1-x}Gd_xO_{3-x/2}$	iv
AB-site	self	$Gd_2O_3 + Ba_{Ba}^{\times} + Ti_{Ti}^{\times} \rightarrow Gd_{Ba}^{\bullet} + Gd_{Ti}^{'} + BaO + TiO_2$ $Ba_{1-y/2}Ti_{1-y/2}Gd_yO_3$	v

The chemical conditions for oxidation and reduction of undoped $BaTiO_3$ are therefore controlled by a combination of the Po_2, temperature, T and time, t, employed during ceramic processing. The oxidation and reduction regimes are separated by a conductivity minimum that corresponds to a p-n transition and gives rise to the intrinsic band gap material described earlier. This minimum is often a broadened region as opposed to a sharp transition and reflects a low level of oxide-ion conduction present. A schematic diagram summarising the σ_b-Po_2 relationship for undoped $BaTiO_3$ at 1200 °C is shown in Fig. 1 (b); the reader is referred to Refs. [14,15] for a full analytical model that explains this observed behaviour and the changes in slopes. It is therefore possible to induce a wide variety of electrical behaviour in $BaTiO_3$, ranging from blue/black n-type semiconducting ceramics to off-white/cream p-type insulating ceramics. With judicious control of Po_2, T and t it is possible to create undoped $BaTiO_3$ ceramics with reduced (n-type) semiconducting grains and oxidised insulating grain boundaries that exhibit the ptcr effect [12].

Trivalent Rare Earth (RE) ions are intermediate in size between Ba and Ti and therefore give rise to various dopant mechanisms dependent on the overall A/B ratio [16–19]. These can give rise to A, B or O-site vacancies or retain the overall ABO_3 stoichiometry. RE doping (typical 0.5–2 mol%) is a key component in obtaining good reliability in highly

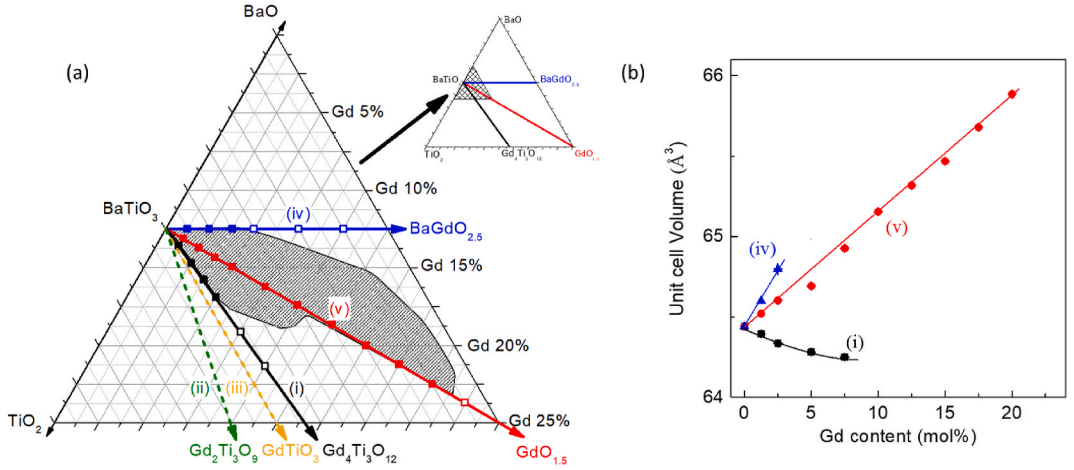

Fig. 2. (a) $BaO–TiO_2$-$GdO_{3/2}$ diagram showing single phase samples (filled symbols) and phase mixtures (open symbols) for samples prepared in air by mechanism (i) at 1450 °C and mechanisms (iv) and (v) at 1550 °C as listed in Table 1. (b) Variation in cell volume versus Gd content for single phase samples by mechanisms (i), (iv) and (v).

insulating $BaTiO_3$-based MLCCs [1–3,20] and A-site doping (typically 0.1 at%) is used to produce ptcr $BaTiO_3$ ceramics [4,21].

Here we use Gd_2O_3 as an intermediate sized RE ion to illustrate the various doping mechanisms that have been proposed for RE-doped $BaTiO_3$, Table 1. The A-site (donor) doping mechanisms are based on ionic compensation through the creation of (i) B or (ii) A site vacancies, or (iii) through electronic compensation with the creation of conduction electrons. Mechanisms (i) and (ii) should result in electrically insulating RT ceramics, given the lack of mobility of A- and B-site metal vacancies at RT, whereas mechanism (iii) should give rise to n-type RT semiconducting ceramics. The B-site (Acceptor) doping mechanism (iv) creates oxygen vacancies and therefore p-type RT insulating ceramics based on the impurity acceptor-doped model are expected. Finally, doping on the A- and B-sites in equal amounts results in the self-compensation mechanism (v) without the creation of any additional ionic or electronic defects and would therefore be expected to have little effect on the conduction properties.

Our approach to study and characterise these doping mechanisms is to:

(a) use equilibrium phase diagrams for samples prepared in air to establish the principal doping mechanisms in Gd-doped $BaTiO_3$ ceramics,

(b) confirm the feasibility of the observed doping mechanism(s) in (a) with atomistic simulations of the energies associated with the various doping mechanisms listed in Table 1,

(c) use impedance spectroscopy, IS, to measure σ_b for the various ceramics,

(d) use Po_2 as a variable to resolve any discrepancies between the observed and/or expected defect mechanisms in (a), (b) and the observed electrical properties from (c).

This approach allows us to illustrate the importance of each method/technique in establishing the electrical properties and how it requires a combination of them all to elucidate the composition-σ_b property relationships of Gd-doped $BaTiO_3$ ceramics. Full experimental details of the ceramic processing conditions used and characterisation methods employed are provided in Supplementary information.

2. Results and discussion

Dense ceramic samples of appropriate composition were prepared at 1450 °C (A-site) or 1550 °C (AB- and B-site) in air corresponding to the five mechanisms listed in Table 1. A summary of the results obtained from X-ray Diffraction (XRD) is shown in the $BaO–TiO_2$-Gd_2O_3 diagram, Fig. 2 (a). The filled symbols represent phase-pure samples based on XRD analysis and show the A-site doping mechanism to be based on the

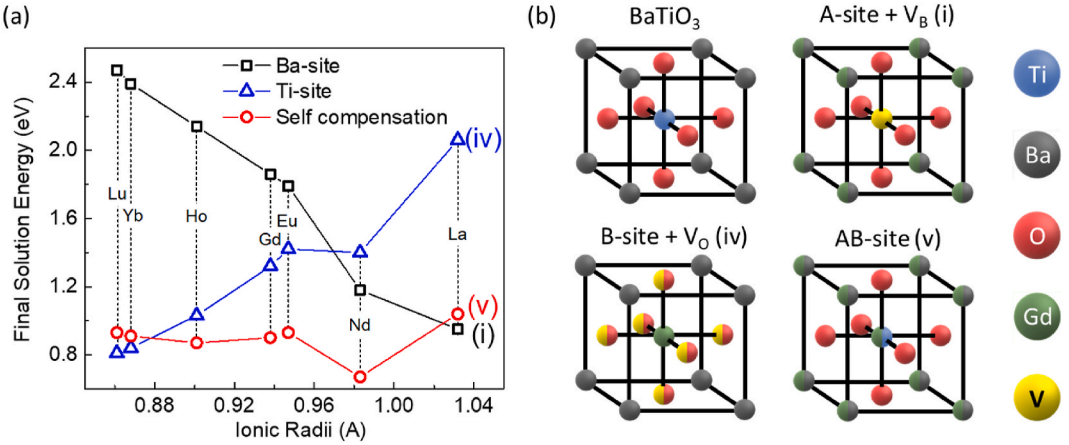

Fig. 3. (a) Variation in final solution energy versus Rare Earth ion radius for mechanisms (i), (iv) and (v). (b) Schematics of the unit cells of undoped $BaTiO_3$, mechanisms (i), (iv) and (v).

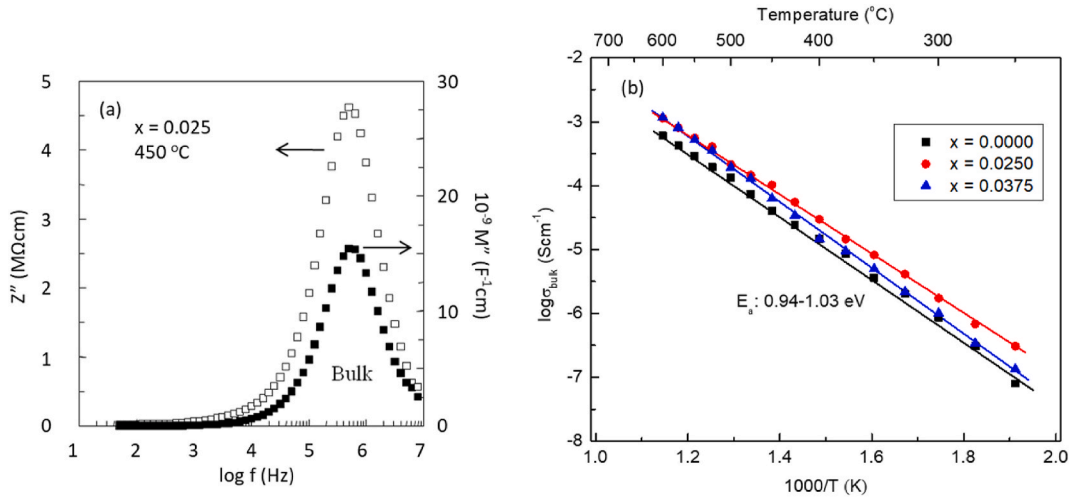

Fig. 4. (a) Z″, M″ spectra for x = 0.025 at 450 °C in air. (b) Arrhenius plots of σ_b for $BaTi_{1-x}Gd_xO_{3-x/2}$ ceramics. (Mechanism iv).

creation of Ti-site vacancies, $Ba_{1-z}Gd_zTi_{1-z/4}O_3$ with $z \leq 0.05$ (black symbols, mechanism (i); the A-B self-compensation mechanism to be the most extensive, $Ba_{1-y/2}Ti_{1-y/2}Gd_yO_3$ with $y \leq 0.20$ (red symbols, mechanism (v); B-site doping with the creation of oxygen vacancies, $BaTi_{1-x}Gd_xO_{3-x/2}$ with $x \leq 0.0375$ (blue symbols, mechanism (iv). All samples prepared by A-site doping with the creation of either A-site vacancies or electronic mechanisms (ii) and (iii) (dashed lines) respectively, were phase mixtures and for simplicity specific compositions have not been included in Fig. 2 (a). Samples were prepared with compositions between those associated with the three principal defect mechanisms to establish the solid solution limits based on variable levels of Ti- and/or oxygen vacancies and are shown by the shaded grey area in Fig. 2 (a). Analysis of the lattice parameters and cell volumes from the XRD data confirm the trends based on ion size effects, Fig. 2 (b). Replacement of the larger Ba ions with smaller Gd ions on the A-site results in a reduction of cell volume (black symbols), whereas the opposite trend for the replacement of smaller Ti with larger Gd on the B-sites results in an expansion of the unit cell (blue symbols). The self-compensation mechanism shows a near-linear increase in cell volume across the solid solution (red symbols).

Freeman et al. [22] developed a set of interatomic potentials to model the defect chemistry of RE-doped $BaTiO_3$ based on the mechanisms listed in Table 1. The values for the final solution energies (i.e. solution energies modified for the most favourable defect binding energies) versus RE ion size based on the three mechanisms in Fig. 2 (a) are shown in Fig. 3. The values vary between ~0.8 and 2.4 eV with the self-compensation mechanism generally having the lowest value across the RE-series. This is in broad agreement with the observation that RE ions, which are intermediate in size between Ba and Ti, can favourably dope onto both sites and therefore form significant self-compensation solid solutions. The influence of RE ion size on the other doping mechanisms can be observed by the A-site doping mechanism with the creation of Ti-site vacancies (mechanism (i), black data points) becoming increasingly favourable (lower in final solution energy) with increasing RE ion size whereas the opposite trend is observed on B-site doping with the creation of oxygen vacancies (mechanism (iv), blue data points), Fig. 2 (a). The extreme A- and B-site doping trends for samples prepared in air based on RE ion size are borne out by experimental data for La which dopes exclusively on the larger A-site [13,23] and for Yb which dopes exclusively on the smaller B-site [18]. All the other RE-ions can form self-compensation solid solutions [16–19].

In the specific case of Gd doping, where the ion size is in the middle of the RE series, it is clear that self-compensation with a final solution energy of ~0.9 eV [22] is strongly favoured, Fig. 3 (a), and this is reflected in the shape and size of the experimentally determined solid solution, Fig. 2 (a). The final solution energies for the A- or B-site mechanisms are larger but comparable, with values of 1.86 and 1.32 eV, respectively [22]. This is consistent with Fig. 3 (a) where these doping mechanisms can occur but to a more limited extent compared to the self-compensation mechanism. The absence of any notable solid solution (s) based on mechanisms (ii) and (iii) for A-site Gd doping is consistent with their larger final solution energies of 2.38 and 10.14 eV, respectively [22]. The final solution energies for all 5 doping mechanisms and more details of the models are given in Ref. [22]. We have omitted the data for mechanisms (ii) and (iii) in Fig. 3 (a) for reasons of conciseness and clarity.

Here we describe the electrical properties of ceramics determined via IS. The data are presented in the form of combined spectroscopic plots of the imaginary components of impedance and electric modulus (so called Z″, M″ spectra). Based on the brick layer model (BLM) of conducting grains ("bricks") and resistive grain boundaries ("mortar"), such analysis can be useful to probe σ_b in homogeneous and heterogeneous electroceramics, as reviewed elsewhere [24–27]. In the BLM, the bulk (grain) response has the lowest capacitance of any electroactive region present and dominates the M″ spectra. A bulk response (to a first approximation) can be modelled on a simple parallel combination of a Resistor (R) and a Capacitor (C) (Fig. S1 (f)) and will give rise to a Debye peak in the M'' (and Z″) spectra and a semi-circular arc in complex M* and Z* plane plots. C (and therefore bulk permittivity) can be calculated as $C = 1/2\ M''_{max}$, based on the M″ peak height, and R, estimated using the relationship $R = 1/(2\pi f_{max}C)$ where f_{max} is the frequency of the peak maximum [28]. If the data have been corrected for the sample geometry, then $\sigma_b \sim 1/R$. A key requirement for the usefulness of IS in extracting σ_b is to ensure that f_{max} for the bulk response occurs in the measured frequency domain, typically between 10^{-2} to 10^6 Hz. If samples are conductive with $R_{RT} < 1$ kΩ, the M″ bulk peak occurs >1 MHz and if they are insulating with $R_{RT} > 100$ MΩ, the M″ bulk peak generally occurs $<10^{-2}$ Hz. To obtain σ_b data therefore requires samples to be cooled below or heated above RT (as appropriate) to ensure f_{max} occurs within the measured frequency range.

Schematic examples of Z″, M″ spectra (and corresponding complex impedance, Z*, plane plots) for a bulk response that occurs within, above and below the measured frequency range are shown in Fig. S1 (a)–(c), respectively. If the ceramics also contain a resistive grain boundary (GB) component, based on the BLM, these can be modelled on a second parallel RC element that is connected in series with the bulk (B) response, Fig. S1 (f). The GB response will also give rise to peaks in Z″ and M″ spectra. This element typically has a higher C and lower f_{max} than the bulk response. Resistive grain boundaries can dominate the Z″ spectra (and Z* plots) but the M″ spectra (and M* plots) still highlight

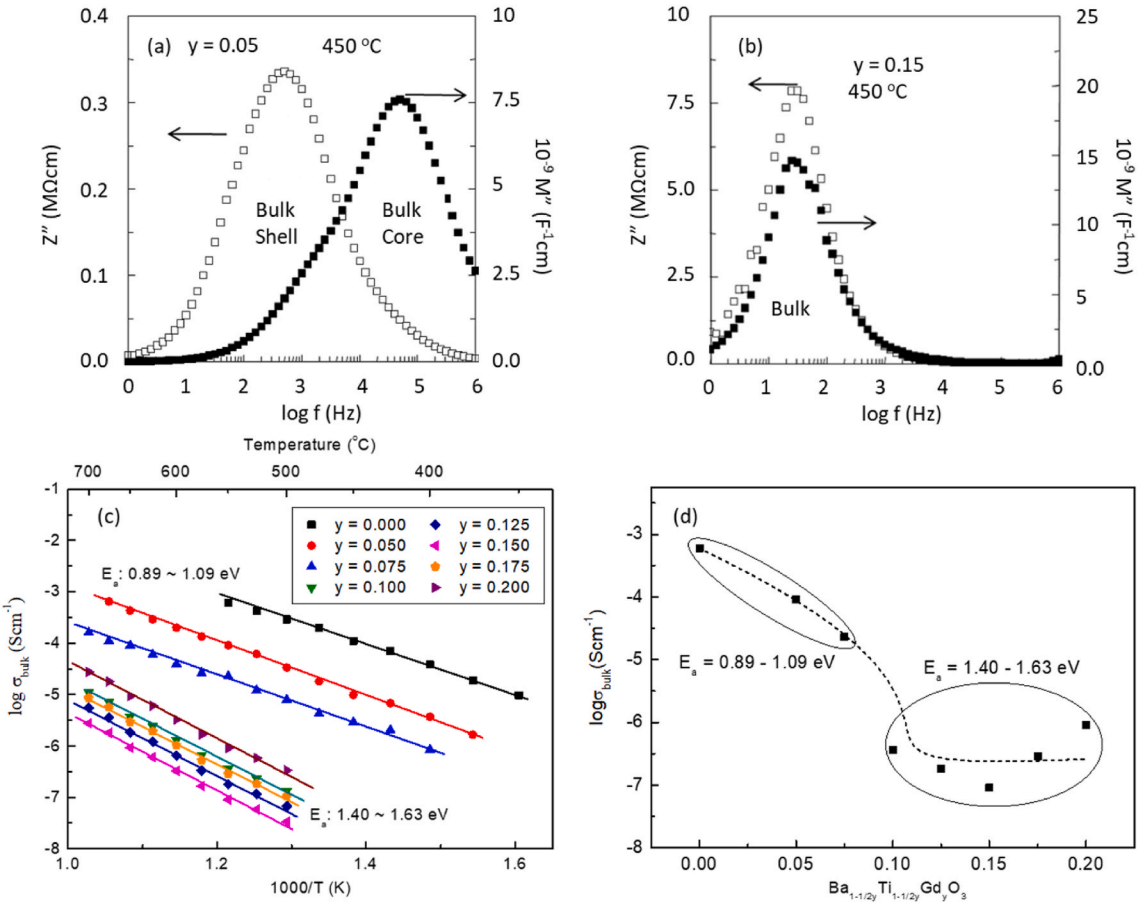

Fig. 5. Z″, M″ spectra for (a) y = 0.05 and (b) 0.15 at 450 °C in air. (c) Arrhenius plots of σ_b for $Ba_{1-y/2}Ti_{1-y/2}Gd_yO_3$ ceramics. (d) Variation in activation energy, E_A, for bulk conduction for $Ba_{1-y/2}Ti_{1-y/2}Gd_yO_3$ ceramics. (Mechanism v).

the bulk response, Fig. S1 (d).

Commercial RE-doped $BaTiO_3$ ceramics for MLCC applications are processed to contain heterogeneous (core-shell, CS) microstructures [1–3,20]. These are based on inner grain cores of $BaTiO_3$ and outer grain shells that contain dopants (including REs) to improve the Temperature Coefficient of Capacitance. In many cases the shell regions are more resistive than the inner grain cores. The individual contributions from these regions to the impedance response can sometimes be resolved using Z″, M″ spectra but often the resolution between the dominant Z'' (shell) and M'' (core) Debye peaks is poor and makes data extraction challenging, Fig. S1 (e). Assessing the geometry and volume fractions of these regions requires analytical electron microscopy to obtain appropriate geometric factors and further complicates any detailed data analysis.

As described above, the electrical properties of BT-based ceramics are controlled by various factors and parameters associated with the raw materials and processing routes. Some doping mechanisms are therefore likely to be more sensitive to these issues than others. To aid comprehension, the results will be discussed in the order of B-site (iv), A- and B-site (v) and A-site (i) Gd-doping. This reflects increasing complexity in correlating the electrical results with the various experimental and computational methods.

2.1. Acceptor, B-site doping, $BaTi_{1-x}Gd_xO_{3-x/2}$ $x \leq 0.0375$: mechanism (iv)

These samples were sintered at 1550 °C in air and are electrically insulating at RT. Higher temperature measurements are required to ensure that the f_{max} associated with the bulk response is in the available frequency domain. The Z″, M″ spectra in Fig. 4 (a) for x = 0.025 at 450 °C show a single peak in Z″ and M″ data with the same f_{max}. This shows that the ceramics are electrically homogeneous (see Fig. S1 (a)) and consist of insulating grains. Arrhenius plots of σ_b show the B-site doped solid solutions to have comparable levels of conductivity and E_A values (~1.0 eV) to undoped $BaTiO_3$ (x = 0) ceramics prepared under the same conditions, Fig. 4 (b). In this case, the behaviour of σ_b under low electric fields is entirely consistent with the well-established extrinsic p-type acceptor model. Although there has to be an increased concentration of oxygen vacancies associated with the Gd-doping compared to undoped $BaTiO_3$, the uptake of oxygen during the cooling cycle after sintering remains small and the additional oxygen vacancies are either associated with the Gd-acceptors (trapped which is supported by the large defect binding energies observed in the atomistic simulations [22]) and/or not mobile under the low electric fields and modest temperatures in which impedance measurements are conducted. As a consequence, acceptor doping on the B-site has negligible influence on σ_b or E_A. There is consistency between the phase equilibrium results, Fig. 2 mechanism (iv), the atomistic simulations, Fig. 3 and the magnitude and type of σ_b, Fig. 4.

2.2. Self-compensation, A + B site doping, $Ba_{1-y/2}Ti_{1-y/2}Gd_yO_3$ $y \leq 0.20$: mechanism (v)

The near-linear variation in cell volume obtained from the phase diagram studies suggests a regular solid solution is formed based on this mechanism, Fig. 2 (b). The extensive nature of this mechanism with a limit of ~20 mol% Gd content is consistent with the atomistic simulations which predict it to be an energetically favourable doping

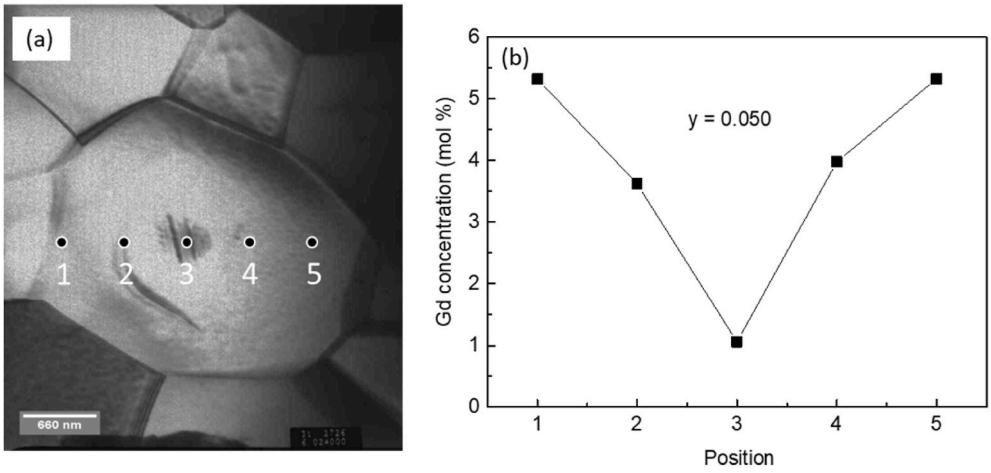

Fig. 6. (a) A bright field TEM image of a core-shell structure of y = 0.05 sintered at 1550 °C in air and (b) Energy Dispersive X-ray analysis on 5 spots in the same grain. (Mechanism v).

mechanism, Fig. 3. In principle, this doping mechanism should not create any additional defects. It is therefore surprising to observe significant differences in the impedance data, Fig. 5 (a, b), σ_b and E_A across this solid solution series, Fig. 5 (c, d), respectively. All samples remain electrically insulating at RT and require impedance measurements at higher temperatures, e.g. 450 °C, to elucidate their electrical microstructures. There is a clear difference in the Z″, M″ spectra for low and high y samples. The former show two, broad, overlapping peaks in each spectrum (y = 0.05, Fig. 5 (a)) indicating a heterogeneous electrical microstructure whereas the latter reveal single, well resolved Z″, M″ Debye peaks with the same f_{max}, (y = 0.15, Fig. 5 (b)) indicating an electrically homogeneous microstructure. These data sets are consistent with a switch over from a core-shell (cs) type response at low doping levels (e.g. y = 0.05, see Fig. S1 (e)) to a single bulk response (e.g. y = 0.15, see Fig. S1 (a)). σ_b decreases with increasing y and reaches a minimum at y = 0.15 (~ four orders of magnitude lower than undoped $BaTiO_3$) before undergoing a modest increase by ~ one order of magnitude towards the end of the solid solution. E_A switches from

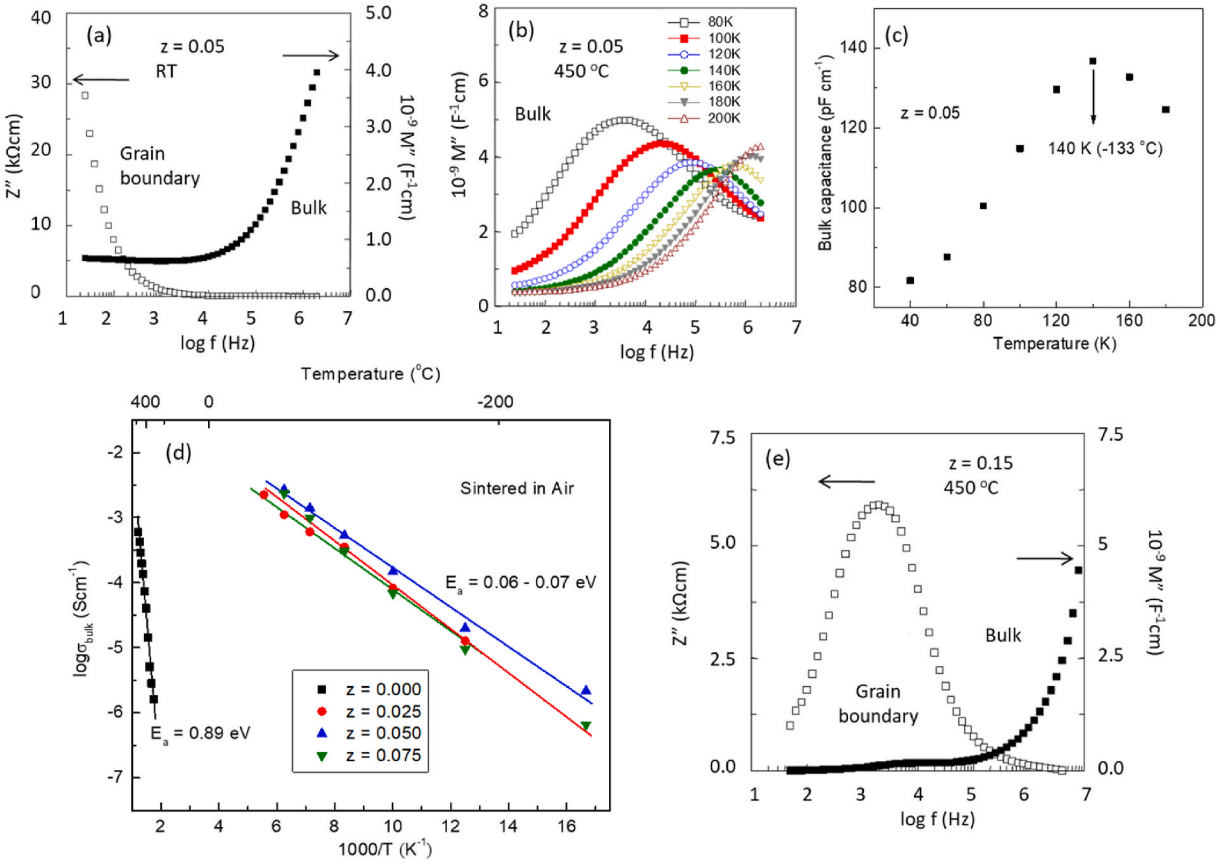

Fig. 7. Various data sets for z = 0.05 ceramics sintered at 1450 °C in air. (a) Z″, M″ spectra at RT; (b) M″ spectra at various sub-ambient temperatures; (c) bulk capacitance versus temperature for z = 0.05; (d) Arrhenius plots of σ_b for $Ba_{1-z}Gd_zTi_{1-z/4}O_3$ ceramics sintered in air at 1450 °C. (e) Z″, M″ spectra for z = 0.05 at 450 °C. (Mechanism i).

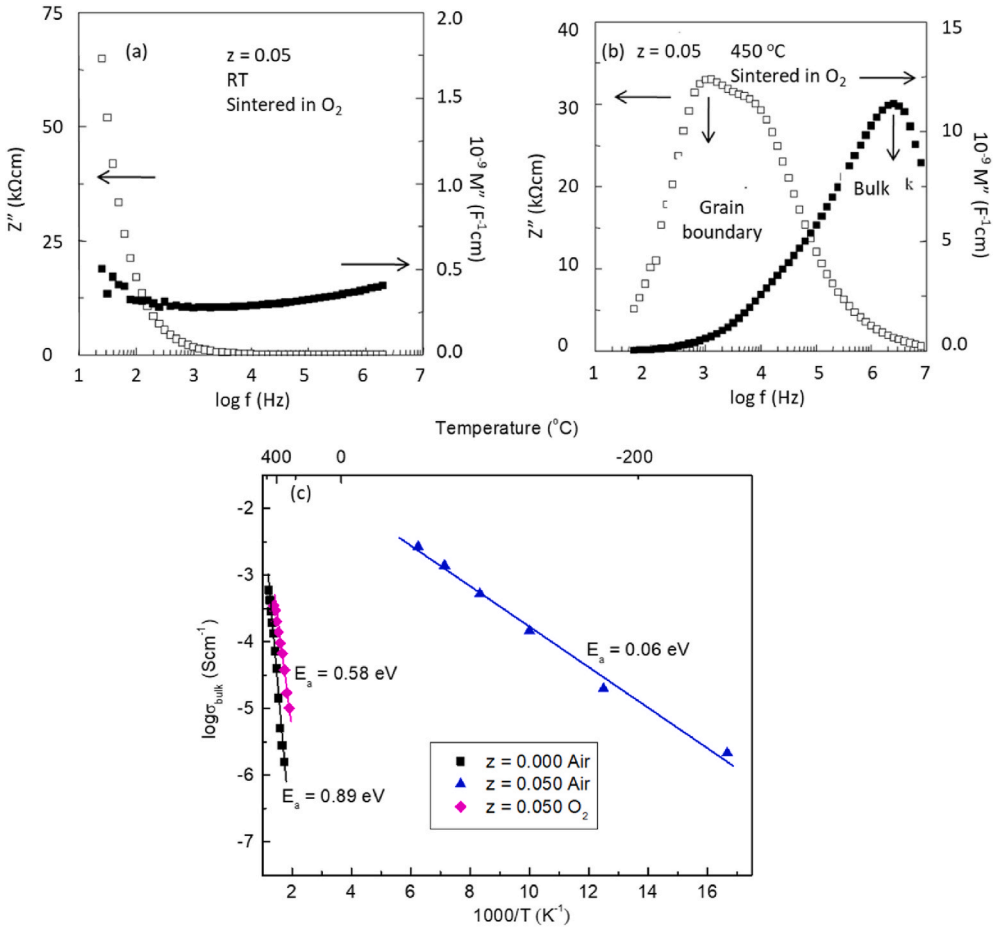

Fig. 8. Z″, M″ spectra for z = 0.05 sintered in O_2 at 1350 °C recorded at (a) RT and (b) 450 °C. Arrhenius plots of σ_b for undoped $BaTiO_3$ sintered in air at 1450 °C (black filled squares), z = 0.05 sintered in air at 1450 °C (filled blue triangles) and z = 0.05 sintered in oxygen at 1350 °C (filled magenta diamonds). (Mechanism i). (For interpretation of the references to colour in this figure legend, the reader is referred to the Web version of this article.)

~0.9–1.1. eV for y ≤ 0.075 to ~1.4–1.6 eV for y > 0.075, Fig. 5 (d).

CS microstructures are a feature of acceptor and donor co-doped $BaTiO_3$, especially at modest doping levels (~1–10 mol%) due to limited diffusion of the dopants. They are commonly created to control the Temperature Coefficient of Capacitance (TCC) in class II $BaTiO_3$-based dielectrics for MLCCs. The impedance data and electrical heterogeneity observed for y = 0.05, Fig. 5 (a), interpreted as a CS-structure was confirmed by analytical Electron Microscopy (see Fig. 6, which clearly showed a high concentration of Gd in the outer grain regions compared to the grain interior, Fig. 6 (b)). Thus, σ_b from the larger and higher frequency M″ peak for y = 0.05 in Fig. 5 (a) can be attributed to extrinsic p-type $BaTiO_3$ (that is primarily undoped) and this is consistent with E_A of ~1.0 eV for y = 0.05, Fig. 5 (c) and (d). Similar behaviour was observed for y = 0.075. The lowering of σ_b from y = 0.00 to 0.075 by ~1.5 orders of magnitude with retention of E_A in the range ~0.9–1.1 eV is attributed to a combination of the variation in current pathways associated with such CS microstructures and the impedance data being corrected for the overall sample geometry as opposed to being corrected for the appropriate volume fraction of the core regions.

The switch to near ideal Z″, M″ spectra observed for y ≥ 0.10, Fig. 5 (b), combined with the lowering of σ_b by three to four orders of magnitude compared to y = 0.00 and the increase in E_A from ~1.0 to > 1.4 eV leads to conduction behaviour that is akin to conduction across the band gap, as described earlier in the scenario of 'ideal' $BaTiO_3$. Achieving this type of behaviour suggests that there is a small excess of Gd-donor doping on the A-site over Gd-acceptor doping on the B-site. This mechanism would allow excess oxygen associated with donor doping to 'fill' residual oxygen vacancies that facilitate the dominant extrinsic p-type behaviour observed in undoped $BaTiO_3$.

$$Gd_2O_3 + 2Ba_{Ba}^{\times} + Vo^{\bullet\bullet} \rightarrow 2Gd_{Ba}^{\bullet} + O_O^{\times} + 2BaO \quad (5)$$

y = 0.15 has the lowest σ_b of all samples and presumably has an oxygen content that is closest to the ideal anion stoichiometry and is therefore the least susceptible to oxidation. The one order of magnitude variation in σ_b for y between 0.10 and 0.20 demonstrates the difficulty in solid state ceramic processing to obtain fully compensated materials that exhibit intrinsic behaviour. It also shows how sensitive electrical measurements are to low levels of non-stoichiometry that are challenging to detect by analytical methods, e.g. small excesses of A- and/or B-site doping and/or detection of solid solution limits.

2.3. Donor, A-site doping, $Ba_{1-z}Gd_zTi_{1-z/4}O_3$ z ≤ 0.05: mechanism (i)

Rare Earth A-site doping of $BaTiO_3$ ceramics processed in air has been a contentious issue for many years, especially in the case of La and the so-called 'donor doping' anomaly [28–33]. It is clear from phase equilibrium studies that Gd-doped materials prepared in air form a measurable solid solution based only on the Ti-vacancy mechanism, $Ba_{1-z}Gd_zTi_{1-z/4}O_3$, Fig. 2. These materials are expected to be electrically insulating and require high temperature measurements to characterise their electrical microstructures. In practice, all ceramics (0 ≤ z ≤ 0.05) sintered in air at 1450 °C are electrically heterogeneous, containing semiconducting and insulating regions. Such spectra are a combination of Fig. S1 (b, c), respectively. RT combined Z″, M spectra for z = 0.05 show the Z″ spectrum is dominated by a low frequency incline with an associated resistivity of ≤10 MΩ cm whereas the M spectrum is

dominated by a high frequency incline with resistivity ≤100 Ω cm, Fig. 7 (a). In addition, the ceramics are much darker in appearance as compared to undoped $BaTiO_3$ and those obtained from self-compensation or acceptor doping.

A broad Debye-like peak in the M″ spectra for z = 0.05 was obtained by cooling below 200 K, Fig. 7 (b). This peak is associated with the bulk response for two reasons: (a) the capacitance obtained from M″ spectra in Fig. 7 (b) was in the range of 80–140 pF cm^{-1} and therefore consistent with a ferroelectric material and (b) the capacitance showed a maximum at 140 K, Fig. 7 (c), which is associated with a sub-ambient polymorphic phase transition in this sample. Arrhenius plots of σ_b for this series of samples are shown in Fig. 7 (d) and all demonstrate a dramatic increase in conductivity compared to undoped $BaTiO_3$ (z = 0) with $E_A \sim 0.1$ eV, indicating n-type bulk semiconductivity.

In contrast, a broad Debye-like peak in the Z″ spectra was obtained by heating samples to temperatures ≥ 300 °C, Fig. 7 (e). This peak is consistent with a resistive grain boundary response as the associated capacitance obtained from the Z″ spectra was ~ 10 nF cm^{-1} (e.g. 13.4 nF cm^{-1} at 450 °C in Fig. 7. (e)), and did not show any evidence of Curie-Weiss (paraelectric) behaviour. Polishing 40% of the pellet thickness (20% from each side of the pellet) showed no significant change in the impedance data between polished and unpolished pellets. This eliminated the possibility that the Z″ spectra were associated with a resistive surface layer on the ceramics. The grain boundary conductivities were similar to those of σ_b for z = 0 and E_A was ~1.2 eV. This analysis shows this series of samples to contain n-type semiconducting grains and insulating grain boundaries.

The clear evidence on n-type semiconducting grains is not consistent with either the equilibrium phase diagram studies or recent atomistic simulations which show the final solution energy for A-site RE electronic donor doping to be in the region of 10 eV [20] and therefore energetically unfavourable compared to the ionic compensation mechanisms shown in Fig. 3. The question now is '*what is the source of the bulk semiconductivity if Gd is not acting as an electronic donor dopant?*' The only other source of n-type semiconductivity in $BaTiO_3$ is based on oxygen-loss, equation (4).

z = 0.05 material was therefore sintered at 1350 °C (and cooled to RT) in flowing O_2 gas. Combined Z″, M″ spectra for RT data are shown in Fig. 8 (a). Both Z″ and M″ spectra were dominated by a low frequency incline with resistivity ≥ 10 MΩ cm at RT. Low temperature impedance (10–320 K) did not show any evidence of a Debye-like peak in the M″ spectra indicating the absence of any semiconducting n-type regions. High temperature impedance data revealed that z = 0.05 sintered in O_2 was electrically heterogeneous, containing at least three regions, as shown in the combined Z″, M″ spectra, Fig. 8 (b), at 450 °C. The Debye-like peak in the M″ spectrum was associated with the bulk response, having a capacitance of ~ 44 pF cm^{-1} while the lower frequency Debye-like peak in the Z″ spectrum was associated with the grain boundary response, having a capacitance of ~ 106 pF cm^{-1}. The existence of a third region was detected by the presence of a "shoulder" at ~ 10^4 Hz in the Z″ spectrum, Fig. 8 (b), whose capacitance and resistivity could not be accurately obtained. However, R and C were estimated to be ~ 60 kΩ cm and ~ 33 pF cm^{-1}, respectively. It is beyond the scope of this script to fully explore the electrical microstructure of these samples but we include this Z″ data to highlight the level of electrical heterogeneity in these samples. E_A for σ_b and the grain boundary conductivity of z = 0.05 sintered in O_2 are shown in Fig. 8 (c). For the bulk, it increased from ~ 0.06 eV for air sintered samples to ~ 0.58 eV. For the grain boundary, E_A was ~ 1.05 eV, similar to that obtained for samples sintered in air.

These results clearly indicate the influence of the processing Po_2 on the electrical properties of these samples. The n-type semiconductivity in the bulk of $Ba_{1-z}Gd_zTi_{1-z/4}O_3$ ceramics processed in air is attributed to a small amount of oxygen-loss during sintering at higher temperature as has been reported in the literature for La-doped ceramics [30–32]. On cooling, oxygen can diffuse into the ceramics via the grain boundaries and therefore the grain boundary regions become oxidised and

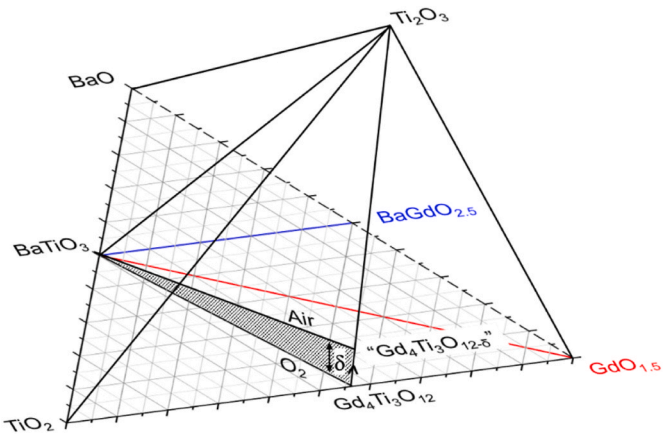

Fig. 9. Schematic of a $BaO\text{-}Gd_2O_3\text{–}TiO_2\text{–}TiO_{3/2}$ quaternary system required to explain the behaviour of σ_b for $Ba_{1-z}Gd_zTi_{1-z/4}O_3$ ceramics sintered in air and O_2. Shaded region is a schematic to illustrate oxygen loss (δ) associated with $Ba_{1-z}Gd_zTi_{1-z/4}O_{3-\delta}$ ceramics processed in air.

electrically insulating. Oxygen loss can be suppressed by processing samples in flowing O_2 gas. When sintered at 1350 °C and cooled to RT in O_2, z = 0.05 did not exhibit any n-type semiconducting regions and showed an insulating bulk response with E_A ~0.58 eV, Fig. 8 (c). These samples are electrically insulating but there is clear heterogeneity associated with their electrical microstructure, Fig. 8 (b), and this is presumably linked to oxygen concentration gradients within these ceramics due to incomplete oxidation.

The reason for the ease of oxygen loss in these ceramics when sintered in air at high temperatures is associated with the doping mechanism. Atomistic simulations have shown that RE doping on the A site, with the creation of titanium vacancies and the loss of lattice oxygen, is energetically more favourable than direct donor electronic doping [34]. For samples processed in air at high temperatures this means the solid solution is more correctly described as $Ba_{1-z}Gd_zTi_{1-z/4}O_{3-\delta}$ where δ is the level of oxygen loss that is dependent on the processing T, t and Po_2. In this case, sintering samples at 1450 °C in air is sufficient to induce δ > 0 and therefore partial reduction of Ti^{4+} to Ti^{3+} to create n-type semiconductivity in the grains with partial reoxidation of the grain boundaries. Sintering the same samples in flowing O_2 at 1350 °C is sufficient to suppress δ to levels such that extrinsic p-type bulk behaviour can be maintained, Fig. 8 (c). This resolves the issue associated with the equilibrium phase diagram because samples prepared in air according to this Ti-vacancy model belong to a quaternary system that includes Ti_2O_3 as a fourth axis to account for oxygen-loss as opposed to being a ternary system with only fully oxidised Ti^{4+} ions as TiO_2, Fig. 9. The shaded region in Fig. 9 is a schematic representation of δ and is the level of oxygen loss associated with $Ba_{1-z}Gd_zTi_{1-z/4}O_{3-\delta}$ ceramics processed in air.

In conclusion, the electrical properties and defect chemistry of Gd-doped $BaTiO_3$ ceramics are strongly dependent on the substitution site of the Gd-dopant as well as the dopant concentration (as exemplified by $Ba_{1-y/2}Ti_{1-y/2}Gd_yO_3$), sintering temperature and atmosphere (as exemplified by $Ba_{1-z}Gd_zTi_{1-z/4}O_3$). We highlight the need for a multi-technique approach involving experimental and computational methods to rationalise the observed electrical properties with the solid solutions formed.

Declaration of competing interest

The authors declare that they have no known competing financial interests or personal relationships that could have appeared to influence the work reported in this paper.

Acknowledgements

We thank the EPSRC Grant No. EP/G005001/1 for funding.

Appendix A. Supplementary data

Supplementary data to this article can be found online at https://doi.org/10.1016/j.oceram.2022.100250.

References

[1] K. Hong, T.H. Lee, J.M. Suh, S.H. Yoon, H.W. Jang, Perspectives and challenges in multilayer ceramic capacitors for next generation electronics, J. Mater. Chem. C. 7 (2019) 9782–9802, https://doi.org/10.1039/c9tc02921d.
[2] M.J. Pan, C. Randall, A brief introduction to ceramic capacitors, IEEE Electr. Insul. Mag. 26 (2010) 44–50, https://doi.org/10.1109/MEI.2010.5482787.
[3] V. Buscaglia, C.A. Randall, Size and scaling effects in barium titanate. An overview, J. Eur. Ceram. Soc. 40 (2020) 3744–3758, https://doi.org/10.1016/J.JEURCERAMSOC.2020.01.021.
[4] B. Huybrechts, K. Ishizaki, M. Takata, The positive temperature coefficient of resistivity in barium titanate, J. Mater. Sci. 30 (1995) 2463–2474, https://doi.org/10.1007/BF00362121.
[5] G.H. Jonker, Some aspects of semiconducting barium titanate, Solid State Electron. 7 (1964) 895–903, https://doi.org/10.1016/0038-1101(64)90068-1.
[6] W. Heywang, Bariumtitanat als sperrschichthalbleiter, Solid State Electron. 3 (1961) 51–58, https://doi.org/10.1016/0038-1101(61)90080-6.
[7] L. Li, B. Walkley, I.M. Reaney, D.C. Sinclair, The influence of Fe_2O_3 reagent grade purity on the electrical properties of 'undoped' $LaFeO_3$ ceramics: a cautionary reminder, J. Eur. Ceram. Soc. 41 (2021) 4189–4198, https://doi.org/10.1016/j.jeurceramsoc.2021.02.019.
[8] I. Wærnhus, P.E. Vullum, R. Holmestad, T. Grande, K. Wiik, Electronic properties of polycrystalline $LaFeO_3$. Part I: experimental results and the qualitative role of Schottky defects, Solid State Ionics 176 (2005) 2783–2790, https://doi.org/10.1016/j.ssi.2005.08.012.
[9] O.P. Thakur, A. Feteira, B. Kundys, D.C. Sinclair, Influence of attrition milling on the electrical properties of undoped-$BaTiO_3$, J. Eur. Ceram. Soc. 27 (2007) 2577–2589, https://doi.org/10.1016/J.JEURCERAMSOC.2006.10.013.
[10] N.-H. Chan, R.K. Sharma, D.M. Smyth, Nonstoichiometry in undoped $BaTiO_3$, J. Am. Ceram. Soc. 64 (1981) 556–562, https://doi.org/10.1111/j.1151-2916.1981.tb10325.x.
[11] N. Masó, H. Beltrán, E. Cordoncillo, A.A. Flores, P. Escribano, D.C. Sinclair, A. R. West, Synthesis and electrical properties of Nb-doped $BaTiO_3$, J. Mater. Chem. 16 (2006) 3114–3119, https://doi.org/10.1039/B601251E.
[12] H. Beltrán, E. Cordoncillo, P. Escribano, D.C. Sinclair, A.R. West, Oxygen loss, semiconductivity, and positive temperature coefficient of resistance behavior in undoped cation-stoichiometric $BaTiO_3$ ceramics, J. Appl. Phys. 98 (2005), 094102, https://doi.org/10.1063/1.2089158.
[13] F.D. Morrison, D.C. Sinclair, A.R. West, Electrical and structural characteristics of lanthanum-doped barium titanate ceramics, J. Appl. Phys. 86 (1999) 6355–6366, https://doi.org/10.1063/1.371698.
[14] N.-H. Chan, R.K. Sharma, D.M. Smyth, Nonstoichiometry in acceptor-doped $BaTiO_3$, J. Am. Ceram. Soc. 65 (1982) 167–170, https://doi.org/10.1111/J.1151-2916.1982.TB10388.X.
[15] D.M. Smyth, The Defect Chemistry of Metal Oxides, Oxford University Press, 2000.
[16] Y. Tsur, T.D. Dunbar, C.A. Randall, Crystal and defect chemistry of rare earth cations in $BaTiO_3$, J. Electroceramics 2001 71 (7) (2001) 25–34, https://doi.org/10.1023/A:1012218826733.
[17] D. Makovec, Z. Samardžija, M. Drofenik, Solid solubility of holmium, yttrium, and dysprosium in $BaTiO_3$, J. Am. Ceram. Soc. 87 (2004) 1324–1329, https://doi.org/10.1111/J.1151-2916.2004.TB07729.X.
[18] L.A. Xue, Y. Chen, R.J. Brook, The effect of lanthanide contraction on grain growth in lanthanide-doped $BaTiO_3$, J. Mater. Sci. Lett. 7 (1988) 1163–1165, https://doi.org/10.1007/BF00722325.
[19] M.T. Buscaglia, V. Buscaglia, M. Viviani, P. Nanni, Atomistic simulation of dopant incorporation in barium titanate, J. Am. Ceram. Soc. 84 (2001) 376–384, https://doi.org/10.1111/J.1151-2916.2001.TB00665.X.
[20] H. Kishi, Y. Mizuno, H. Chazono, Base-metal electrode-multilayer ceramic capacitors: past, present and future perspectives, Jpn. J. Appl. Phys. 42 (2003) 1–15, https://doi.org/10.1143/JJAP.42.1.
[21] G.V. Lewis, C.R.A. Catlow, R.E.W. Casselton, PTCR effect in $BaTiO_3$, J. Am. Ceram. Soc. 68 (1985) 555–558, https://doi.org/10.1111/J.1151-2916.1985.TB11523.X.
[22] C.L. Freeman, J.A. Dawson, H.-R. Chen, J.H. Harding, L.-B. Ben, D.C. Sinclair, A new potential model for barium titanate and its implications for rare-earth doping, J. Mater. Chem. 21 (2011) 4861–4868, https://doi.org/10.1039/C0JM04058D.
[23] F.D. Morrison, D.C. Sinclair, J.M.S. Skakle, A.R. West, Novel doping mechanism for very-high-permittivity barium titanate ceramics, J. Am. Ceram. Soc. 81 (1998) 1957–1960, https://doi.org/10.1111/J.1151-2916.1998.TB02575.X.
[24] N.M. Beekmans, L. Heyne, Correlation between impedance, microstructure and composition of calcia-stabilized zirconia, Electrochim. Acta 21 (1976) 303–310, https://doi.org/10.1016/0013-4686(76)80024-2.
[25] J.R. Macdonald, Impedance Spectroscopy, John Wiley & Sons, Now York, 1987.
[26] J.T.S. Irvine, D.C. Sinclair, A.R. West, Electroceramics: characterization by impedance spectroscopy, Adv. Mater. 2 (1990) 132–138, https://doi.org/10.1002/adma.19900020304.
[27] J.P. Heath, J.H. Harding, D.C. Sinclair, J.S. Dean, The analysis of impedance spectra for core–shell microstructures: why a multiformalism approach is essential, Adv. Funct. Mater. 29 (2019) 1904036, https://doi.org/10.1002/adfm.201904036.
[28] D.C. Sinclair, A.R. West, Impedance and modulus spectroscopy of semiconducting $BaTiO_3$ showing positive temperature coefficient of resistance, J. Appl. Phys. 66 (1989) 3850–3856, https://doi.org/10.1063/1.344049.
[29] H.M. Chan, M.R. Harmer, D.M. Smyth, Compensating defects in highly donor-doped $BaTiO_3$, J. Am. Ceram. Soc. 69 (1986) 507–510, https://doi.org/10.1111/J.1151-2916.1986.TB07453.X.
[30] F.D. Morrison, A.M. Coats, D.C. Sinclair, A.R. West, Charge compensation mechanisms in La-doped $BaTiO_3$, J. Electroceram. 6 (2001) 219–232, https://doi.org/10.1023/A:1011400630449.
[31] F.D. Morrison, D.C. Sinclair, A.R. West, Doping mechanisms and electrical properties of La-doped $BaTiO_3$ ceramics, Int. J. Inorg. Mater. (2001) 1205–1210, https://doi.org/10.1016/S1466-6049(01)00128-3.
[32] F.D. Morrison, D.C. Sinclair, A.R. West, An alternative explanation for the origin of the resistivity anomaly in La-doped $BaTiO_3$, J. Am. Ceram. Soc. 76 (2001) 474–476, https://doi.org/10.1111/j.1151-2916.2001.tb00684.x.
[33] D.M. Smyth, The defect chemistry of donor-doped $BaTiO_3$: a rebuttal, J. Electroceram. 9 (2002) 179–186, https://doi.org/10.1023/A:1023213208904.
[34] C.L. Freeman, J.A. Dawson, H.-R. Chen, L. Ben, J.H. Harding, F.D. Morrison, D. C. Sinclair, A.R. West, Energetics of donor-doping, metal vacancies, and oxygen-loss in A-site rare-earth-doped $BaTiO_3$, Adv. Funct. Mater. 23 (2013) 3925–3938, https://doi.org/10.1002/ADFM.201203147.